ACS NANO

www.acsnano.org

ARTICLE

# Structural Basis for Alternative Self-Assembly Pathways Leading to Different Human Immunodeficiency Virus Capsid-Like Nanoparticles

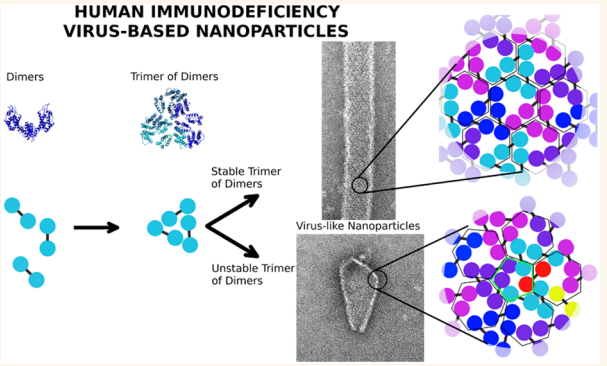
Judith Escrig, íñigo Marcos-Alcalde, Santos Domínguez-Zotes, David Abia, Paulino Gómez-Puertas, Alejandro Valbuena,* and Mauricio G. Mateu*

Cite This: *ACS Nano* 2024, 18, 27465−27478

Read Online

ACCESS | Metrics & More | Article Recommendations | Supporting Information

**ABSTRACT:** **The mechanisms that underlie the spontaneous and faithful assembly of virus particles are guiding the design of self-assembling protein-based nanostructures for biomedical or nanotechnological uses. In this study, the human immunodeficiency virus (HIV-1) capsid was used as a model to investigate what molecular feature(s) may determine whether a protein nanoparticle with the intended architecture, instead of an aberrant particle, will be self-assembled *in vitro*. Attempts of using the HIV-1 capsid protein CA for achieving *in vitro* the self-assembly of cone-shaped nanoparticles that contain CA hexamers and pentamers, similar to authentic viral capsids, had typically yielded hexamer-only tubular particles. We hypothesized that a reduction in the stability of a transient major assembly intermediate, a trimer of CA dimers (ToD), will increase the propensity of CA to assemble *in vitro* into cone-shaped particles instead of tubes. Certain amino acid substitutions at CA-CA interfaces strongly favored *in vitro* the assembly of cone-shaped nanoparticles that resembled authentic HIV-1 capsids. All-atom MD simulations indicated that ToDs formed by CA mutants with increased propensity for assembly into cone-shaped particles are destabilized relative to ToDs formed by wt CA or by another mutant that assembles into tubes. The results also indicated that ToD destabilization is mediated by conformational distortion of different CA−CA interfaces, which removes some interprotein interactions within the ToD. A model is proposed to rationalize the linkage between reduced ToD stability and increased propensity for the formation of CA pentamers during particle growth *in vitro*, favoring the assembly of cone-shaped HIV-1 capsid-like nanoparticles.**




**KEYWORDS:** *nanoparticle, virus capsid, self-assembly, assembly pathways, architecture, mutational analysis, molecular dynamics*

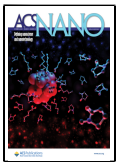
Downloaded via CSIC on March 31, 2025 at 07:19:56 (UTC).
See https://pubs.acs.org/sharingguidelines for options on how to legitimately share published articles.

## INTRODUCTION

Protein-based nanostructures are being designed and engineered for many developing applications in biomedicine or nanotechnology. Those nanostructures are ideally built using a bottom-up approach, in which free protein molecules are made to spontaneously assemble into a nanoparticle with a certain size and architecture.[1−6] Inspiration and knowledge to design self-assembling protein-based nanostructures is coming in large part from the study of the spontaneous assembly of the capsids of many viruses.[7−13]

Biological evolution has endowed viral capsid proteins with the information required for their self-association into natural nanoparticles with defined sizes and architectures as well as outstanding properties and complex functions. Virus capsid self-assembly from protein building blocks generally involves an efficient chain of molecular recognition events that proceed along a favorable energy gradient.[11,12] However, the path for the formation of a virus capsid with the biologically correct structure is fraught with danger: competing association reactions may easily result in aggregated, misassembled, or incomplete virus particles that are noninfectious. Minor

Received: June 14, 2024
Revised: September 9, 2024
Accepted: September 12, 2024
Published: September 27, 2024



ACS Publications

© 2024 American Chemical Society

structural changes in the viral capsid proteins or small variations in physical or chemical conditions are frequently enough to favor off-pathway assembly intermediates and dead-ends.[11,14,15] In the face of strong selection pressures, many viruses have evolved auxiliary machinery and subverted cellular resources for achieving a carefully regulated, faithful capsid assembly process under the demanding conditions found in their host cells.[15−17]

Self-assembly of a number of virus capsids or virus-like particles (VLPs) has been achieved *in vitro* using capsid protein subunits in the absence of any other biomolecule.[10−13,18−25] In some cases, particles that were indistinguishable from authentic virus capsids were obtained, but the physical and chemical conditions required were very different from those found *in vivo*. In other cases, the size and architecture of the assembled particles were different from those of the authentic virus capsids. *In vitro* viral capsid assembly systems are most suitable to investigate which structural features of the building blocks and physical or chemical conditions may determine the self-assembly of a protein-based nanoparticle with the desired architecture instead of an aberrant protein complex. These studies are, thus, most important for achieving and improving the production of virus-based nanoparticles and nanomaterials for biomedical or industrial uses.[26,27] They can also provide critical guidelines for achieving the efficient and faithful assembly of protein-based nanostructures with the desired architecture.

The capsid of the mature human immunodeficiency virus type 1 (HIV-1)[28] provides an excellent *in vitro* model system to explore the structural features and conditions that determine the correct assembly of a protein-based nanoparticle of complex architecture. The mature HIV-1 capsid is made of many copies of a single viral protein, capsid protein CA (Figure 1A). CA is composed of a N-terminal domain (NTD) linked by a flexible peptide region to a C-terminal domain (CTD). The capsid formed in the maturing HIV-1 virion is fundamentally made of a hexagonal lattice of CA protein subunits (Figure 1B). The subunits within each CA hexamer in the lattice are noncovalently bound through NTD−NTD and NTD−CTD interfaces, whereas each hexamer is noncovalently associated with the 6 neighbor hexamers through CTD−CTD interfaces (Figure 1B).[28] The particular lattice curvature required to form the closed, truncated cone-shaped mature HIV-1 capsid within the maturing virion is achieved by the formation of 12 CA pentamer "defects" at certain positions in the hexamer-based protein lattice (Figure 1C).[28]

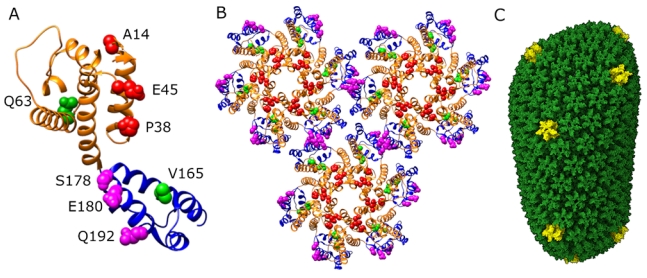



**Figure 1. Structure of the mature HIV-1 capsid. (A) ribbon model of the structure of a CA monomer with the NTD and CTD, respectively, colored orange and blue (PDB ID: 4xfx). The residues at CA−CA interfaces in the capsid protein lattice that were chosen for mutational analysis are indicated as space-filling models and color-coded: red, residues at NTD−NTD interfaces; green, residues at NTD−CTD interfaces; purple, residues at CTD−CTD interfaces. (B) three hexamers in the CA lattice. The CA amino acid residues chosen for mutational analysis are represented and colored as in panel (A). NTD−NTD, NTD−CTD, and CTD−CTD interfaces correspond to the interdomain regions that, respectively, include the red, green, or purple residues represented and chosen for mutational analysis in this study. (C) mature HIV-1 capsid architecture (PDB ID 3j3y). CA hexamers and pentamers are, respectively, colored green and yellow.**

In contrast to the situation in the maturing HIV-1 virion, free CA from HIV-1 *in vitro*, in the absence of any other biomolecules, is unable to self-assemble at close to physiological ionic strength. *In vitro*, self-assembly of CA (without any additional sequence from the Gag precursor) is typically achieved using a very high ionic strength,[21,29] which screens ionic repulsions between the CA building blocks.[30,31] Alternatively, CA self-assembly *in vitro* can be promoted at close to physiological ionic strength by a macromolecular crowding agent that increases the CA activity (effective concentration) through an excluded volume effect.[32] In the maturing virion, capsid assembly can occur at a physiologic ionic strength in the confined and crowded space inside the matrix protein (MA) shell under the viral envelope. In addition, CA−CA repulsions may be screened in the virion by counter charges on the nucleocapsid (NC) protein-viral RNA complex.[33]

The different conditions needed for the self-assembly of CA alone *in vitro* relative to those found in the maturing virion lead to different particle architectures. Instead of cone-shaped capsids, at a high ionic strength or in the presence of a crowding agent *in vitro*, long, hollow cylinders (tubes) with open ends are generally formed.[21,29−32] Flat or partially rolled sheets were also observed in some cases.[34] Both sheets and tubes (i.e., sheets rolled into a cylinder) are morphologies made of a regular lattice of CA hexamers, without a need for including pentamer defects (Figure S1, top images). In addition to many tubular particles, free CA from HIV-1 occasionally formed *in vitro* a few truncated cone-shaped particles that resembled authentic capsids, for example when a macromolecular crowding agent was used[32] (Figure S1, bottom left image). Together, the results showed that the propensity of HIV-1 CA to form pentamer-containing, cone-shaped capsids is very much reduced when it is assembled in an unconfined, high ionic strength *in vitro* environment instead than under the conditions found inside the virion.

Different amino acid substitutions or disulfide cross-links have been introduced in CA oligomers of HIV-1 to study certain structural features or functions of the mature HIV-1 capsid. Some of those structural modifications significantly increased, during *in vitro* assembly of free CA, the proportion of cone-shaped particles or other morphologies that require the presence of pentamers (Figure S1, bottom images), instead of exclusively forming hexamer-only tubes.[35,36] Those structural modifications in CA thus appeared to promote the formation of pentameric defects in the CA protein lattice under the tested *in vitro* conditions.

In solution, HIV-1 CA monomers and dimers are in equilibrium, with the dimer being the dominant initial capsid building block at protein concentrations >100 $\mu$M. Both theoretical considerations and experimental evidence support the proposal that a trimer of CA dimers (ToD) is a major transient intermediate for assembly of the mature HIV-1 capsid


https://doi.org/10.1021/acsnano.4c07948
ACS Nano 2024, 18, 27465−27478

(Figure 2A).[37−39] Tsiang et al.[38] proposed a theoretical model that involves the critical existence of a ToD intermediate,

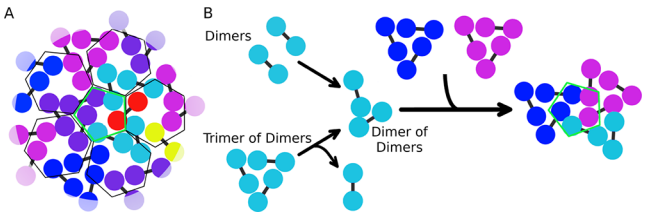



**Figure 2. Pentagonal defects in the mature HIV-1 hexagonal capsid lattice. CA dimers are represented as dumbbells, with circles and sticks, respectively, representing the NTD and CTD domains of the two bound CA monomers in a dimer.[38] (A) a CA pentamer (oulined in green) surrounded by CA hexamers in the capsid lattice. ToDs are represented in different colors. A CA dimer (colored red) is shared by two neighboring ToDs (cyan), giving rise to the formation of a pentamer defect in the hexagonal lattice. (B) Two possible pathways for the formation of a CA pentamer during assembly of the mature HIV-1 capsid: (i) a transient dimer of dimers (DoD) may associate with two ToDs before a third dimer could bind the DoD to complete a ToD; (ii) a dimer could dissociate from a preformed ToD, leaving a transient DoD that may associate with two ToDs before another dimer could bind the DoD. In both cases, a CA pentamer would be formed in the growing protein lattice.**

which was supported by experimental evidence provided by fitting of capsid assembly kinetic curves. Summers et al.[39] introduced mutations in CA that led to the experimental identification of a ToD intermediate of HIV-1 capsid assembly. However, growth by association of just ToDs would result in a regular hexagonal lattice with no pentagonal defects, as in the tubes and sheets formed by CA *in vitro*. How and under which conditions CA pentamers can be formed during assembly of the hexagonal lattice to yield authentic, cone-shaped HIV-1 capsids was unclear.

Here we formulate and test the hypothesis that, under conditions required for assembly of HIV-1 CA *in vitro*, structural modifications introduced in the CA protein that destabilize the ToD intermediate may promote the formation of pentameric defects during growth of the hexameric CA lattice. We consider that a pentamer could be formed in the growing lattice by association between a transient dimer of dimers (DoD) and two ToDs, as indicated in Figure 2B. A reduction in ToD stability will favor dissociation of a CA dimer from a preformed ToD and/or impair the association of a CA dimer with a transient DoD to yield a ToD. The increased population of transient DoDs will increase the probability of formation of a pentamer in the growing CA lattice (Figure 2B). This working hypothesis predicts that those amino acid substitutions in CA that reduce ToD stability will increase the propensity of CA to assemble into cone-shaped nanoparticles instead of nanotubes. In this study, we have subjected this hypothesis to verification by using a series of CA mutants for both experimental analyses and all-atom molecular dynamics (MD) simulations.

## RESULTS AND DISCUSSION

**Selection of Amino Acid Residues at Protein−Protein Interfaces in the HIV-1 CA Lattice for Mutation to Alanine.** We determined first the differences in assembly, disassembly, and morphology of HIV-1 CA VLPs when specific noncovalent interactions between subunits in the capsid protein lattice were removed. Removal of specific interactions was achieved by individual mutation to alanine of 7 chosen amino acid residues located at protein−protein interfaces in the CA lattice. Those 7 residues were located either at interfaces within each CA hexamer (2 residues at each NTD−NTD interface, and 2 other residues at each NTD−CTD interface), or at CTD−CTD interfaces between hexamers (3 residues) (Figure 1). Those residues were chosen for mutation because: (i) truncation of their side chain by mutation to alanine would remove multiple intersubunit interactions in the CA lattice, including hydrogen bonds, ionic bonds, and/or multiple van der Waals contacts (including in some cases carbon−carbon "hydrophobic" contacts) (Table S1). (ii) They are highly conserved among HIV-1 variants (Table S1), which suggests they have a biological role. (iii) they were shown to have a role in maintaining the stability of the HIV-1 core (the mature capsid containing the nucleoprotein complex)[40,41] and/or the oligomerization affinity between CA subunits.[42]

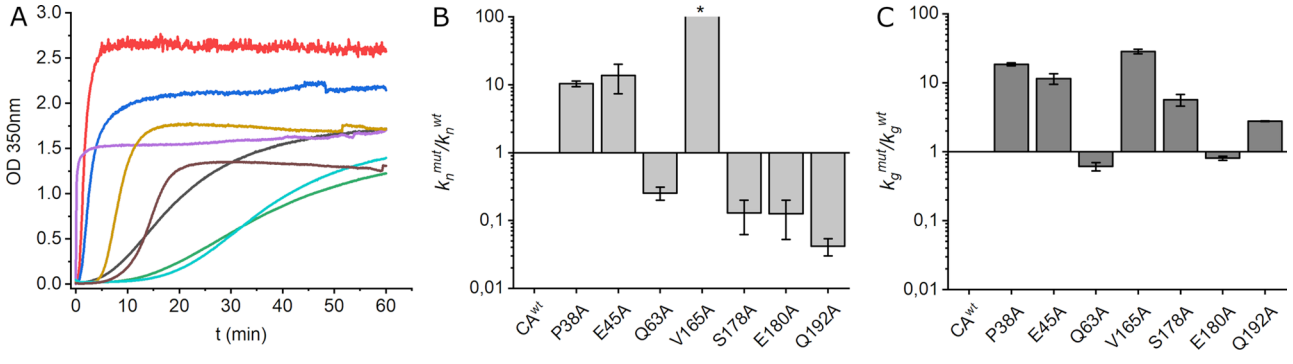



**Figure 3. Comparative self-assembly kinetics of wt and alanine mutant CAs. (A) Effects on the kinetics of CA self-assembly by the individual mutation of different interfacial amino acid residues to alanine. CA polymerization was followed by monitoring of the optical density (OD) at 350 nm. The curve corresponding to each variant protein in a representative experiment is color coded (dark gray, wt CA; brown, Q192A; green, Q63A; cyan, E180A; orange, S178A; blue, E45A; red, P38A; purple, V165A). (B) Bar plot of the ratio between the nucleation rate constant $k_n$ for each mutant CA and the $k_n$ for wt CA, averaged from data obtained in duplicate experiments ($k_n^{wt}$ = 0.013 ± 0.002 $min^{-1}$). For mutant V165A a minimum value is given (indicated by an asterisk), as the nucleation rate was faster than the experimental dead time. (C) Bar plot of the ratio between the growth rate constant $k_g$ for each mutant CA and the $k_g$ for wt CA, averaged from data obtained in duplicate experiments ($k_g^{wt}$ = 0.059 ± 0.003 OD·$min^{-1}$). Error bars in (B) and (C) correspond to standard deviations.**



https://doi.org/10.1021/acsnano.4c07948
ACS Nano 2024, 18, 27465−27478

The chosen mutations were introduced into CA by site-directed mutagenesis. The nonmutated (wt) and mutant CA proteins were expressed and purified as described in Methods, and they were analyzed as described next.

**Changes in VLP Assembly Kinetics by Truncating Specific Side Chains at Interfaces in the CA Lattice.** Assembly of wt and each mutant VLP at pH 7.4 was done at the same protein concentration, under the same experimental conditions. The reaction was triggered by increasing the salt concentration (to 2.25 M NaCl), and the amount of assembled CA as a function of time was followed by turbidimetry, as described previously[29,32] (see Methods) (Figure 3). The result of a representative experiment is shown in Figure 3A. The reaction kinetic parameters for the wt CA and each tested mutant CA were obtained by fitting the experimental data to a sigmoidal nucleation and growth process.[43] For each tested VLP, the values for the nucleation rate constant, $k_n$, and the growth rate constant, $k_g$, were obtained in duplicate experiments, normalized relative to the corresponding wt values and averaged. Average relative $k_n$ and $k_g$ values and associated errors are respectively shown in Figure 3B,C. It was not possible to precisely determine the nucleation rate constant for the V165A mutant, because the nucleation reaction was faster than the experimental dead time (~6 s). However, the data did reveal that for V165A $k_n$ was at least 2 orders of magnitude higher than the wt.

The results (Figure 3) showed that 3 out of the 7 mutant CAs nucleated and grew much faster than wt CA (growth rate constant $k_g$ 11.5× (E45A), 18.5× (P38A), or 28× (V165A) that of the wt). Two other mutants nucleated at a slower rate, but still grew faster than the wt ($k_g$ 2.7× (Q192A) or 5.6× (S178A) that of the wt). Only two mutants both nucleated and grew at (somewhat) slower rates than the wt ($k_g$ 0.6× (Q63A) or 0.8× (E180A) that of the wt).

**Changes in VLP Disassembly Kinetics by Truncating Specific Side Chains at Interfaces in the CA Lattice.** Disassembly of the previously assembled wt and mutant VLPs at pH = 7.4 was done at the same protein concentration and under the same experimental conditions. The reaction was triggered by a 10-fold reduction in the total protein concentration by dilution with the same buffer, and the amount of assembled VLPs remaining as a function of time was followed by turbidimetry, as described previously[31] (see Methods) (Figure 4). The result of a representative experiment is shown in Figure 4A. The reaction kinetic parameters for the wt CA and each tested mutant CA were obtained by fitting the experimental data to an exponential decay process. For each tested VLP, the value for the disassembly rate constant, $k_d$, was obtained in 3 duplicate experiments, normalized relative to the corresponding wt value, and averaged. Average relative $k_d$ values and associated errors are shown in Figure 4B.

The results showed that 2 out of the 7 CA mutants disassembled faster than the wt, with a $k_d$ 3.4× (Q63A) or 3.9× (P38A) that of the wt. Four mutants (E45A, S178A, E180A, and Q192A) disassembled with a rate similar to the wt. One mutant (V165A) disassembled at a slower rate than the wt (0.2× the wt rate).

To sum up, the results of comparative kinetic analyses revealed that every tested mutation influenced the CA self-assembly rate (both nucleation and growth rate) and, in some cases, also the disassembly rate, and the effects of most mutations were different. A broad categorization for the 7 tested alanine mutations in CA could be established considering their influence on the (dis)assembly kinetics:

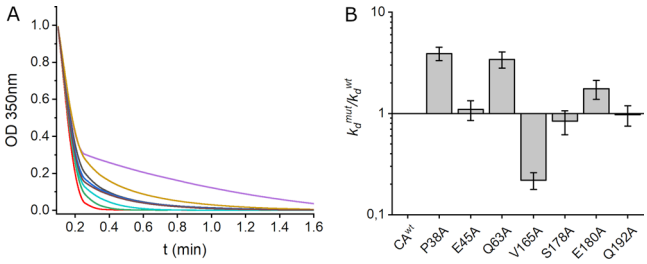



**Figure 4. Comparative disassembly kinetics of wt and alanine mutant CA particles. (A) Effects on the kinetics of CA particle disassembly by the individual mutation of different interfacial amino acid residues to alanine. Disassembly of polymerized VLPs was followed by monitoring the OD at 350 nm. The curve corresponding to each variant CA in a representative experiment is color coded (dark gray, CA wt; brown, Q192A; green, Q63A; cyan, E180A; orange, S178A; blue, E45A; red, P38A; purple, V165A). (B) bar plot of the ratio between the disassembly rate constant $k_d$ for each mutant CA and the $k_d$ for wt CA, averaged from data obtained in triplicate experiments ($k_d^{wt}$ = 0.07 ± 0.02 min$^{-1}$). Error bars correspond to standard deviations.**

Group I, mutants with a lesser influence: E45A at the NTD−NTD interface and S178A, E180A, and Q192A at the CTD−CTD interface assembled either faster or slower than the wt, but disassembled at a similar rate. The similar dissociation kinetics obtained for group I mutant VLPs and the wt VLP suggested that they all could form particles with the same structural organization (i.e, mainly tubes).

Group II, mutants which exerted conspicuous (though different) effects: V165A at the NTD−CTD interface assembled much faster than the wt and disassembled at a slower rate; Q63A, also at the NTD−CTD interface, assembled somewhat slower than the wt and disassembled at a faster rate; P38A, at the NTD−NTD interface, assembled and disassembled faster than the wt. The conspicuous assembly kinetics differences between group II mutant CAs and wt CA suggested that they could form VLPs that differ from the wt VLP not only in stability, but also in structural organization.

**Changes of VLP Architecture by Truncating Specific Side Chains at Interfaces in the CA Lattice.** The morphologies and dimensions of the assembled wt and mutant VLPs were then determined by TEM imaging of many individual particles in each case, using negative staining (see Methods) (Figure 5). Nearly all individual VLPs assembled from wt CA and observed by TEM corresponded to long tubes (Figure 5); occasionally, some flat sheets were observed. Similar results had previously been obtained by us and other groups that investigated assembly of the wt HIV-1 CA *in vitro*, under conditions similar to those used in the present study (see for example ref.[32]).

The alanine mutant VLPs tested here showed different morphologies, or mixtures of different morphologies, depending on the mutant (Figure 5). The different observed morphologies were grouped as follows (Figure S1):

Type H: morphologies that were previously shown to be based on a regular hexameric lattice (Figure S1, top images), without a requirement for the formation of pentameric defects.[29] This type included tubes (i.e., rolled sheets), flat sheets, and, occasionally, partially rolled sheets.


https://doi.org/10.1021/acsnano.4c07948
ACS Nano 2024, 18, 27465−27478

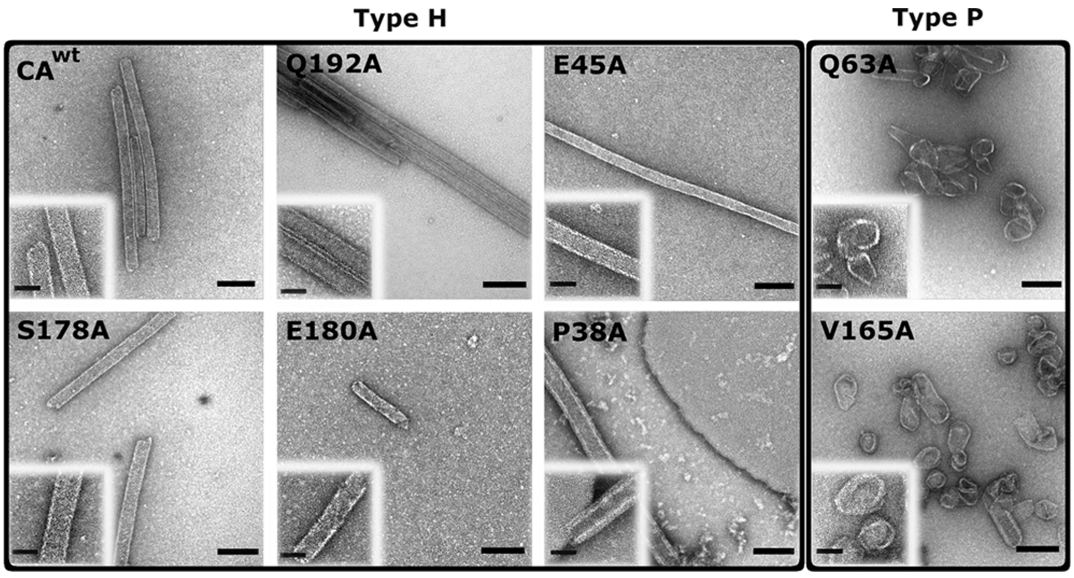



**Figure 5. Visualization by TEM of wt and alanine mutant VLPs self-assembled *in vitro*. The scale bars represent a length of 150 nm. The scale bars in the insets represent 50 nm.**

**Table 1. Quantification and Characterization of CA VLPs Obtained in *In Vitro* Assembly Experiments**

| | Percentages (%)[a] | | | | Dimensions (nm)[b] | | | | | | | |
|---|---|---|---|---|---|---|---|---|---|---|---|---|
| | Type H | | Type P | | Type H | | Type P | | | | | |
| Protein | Tubes | Sheets | Cones | Spheres | $D_{tubes}$ | N | $L_{cones}$ | N | $D_{max,cones}$ | N | $D_{spheres}$ | N |
| $CA^{wt}$ | 95 | 5 | 0 | 0 | 49 ± 5 | 60 | | | | | | |
| P38A | 28 | 72 | 0 | 0 | 54 ± 14 | 13 | | | | | | |
| E45A | 100 | 0 | 0 | 0 | 48 ± 6 | 41 | | | | | | |
| S178A | 100 | 0 | 0 | 0 | 48 ± 5 | 54 | | | | | | |
| E180A | 100 | 0 | 0 | 0 | 41 ± 4 | 53 | | | | | | |
| Q192A | 97 | 3 | 0 | 0 | 50 ± 5 | 66 | | | | | | |
| Q63A | 17 | 0 | 71 | 12 | 51 ± 8 | 15 | 120 ± 28 | 28 | 68 ± 8 | 28 | 65 ± 9 | 4 |
| V165A | 8 | 0 | 87 | 5 | 59 ± 7 | 28 | 110 ± 23 | 82 | 68 ± 13 | 82 | 60 ± 9 | 21 |
| $CA^{wt}{}_{r}$ | 100 | 0 | 0 | 0 | 46 ± 4 | 20 | | | | | | |
| $CA^{wt}{}_{nr}$ | 100 | 0 | 0 | 0 | 48 ± 7 | 23 | | | | | | |
| $CA^{1m}{}_{r}$ | 100 | 0 | 0 | 0 | 57 ± 12 | 31 | | | | | | |
| $CA^{1m}{}_{nr}$ | 100 | 0 | 0 | 0 | 49 ± 8 | 51 | | | | | | |
| $CA^{2m}{}_{r}$ | 13 | 0 | 75 | 12 | 54 ± 5 | 25 | 85 ± 13 | 35 | 53 ± 8 | 35 | 52 ± 7 | 18 |
| $CA^{2m}{}_{nr}$ | 8 | 0 | 82 | 10 | 53 ± 6 | 32 | 84 ± 12 | 38 | 51 ± 9 | 38 | 50 ± 6 | 17 |
| $CA^{3m}{}_{r}$ | 37 | 0 | 50 | 13 | 56 ± 7 | 21 | 74 ± 11 | 20 | 45 ± 6 | 20 | 51 ± 9 | 16 |
| $CA^{3m}{}_{nr}$ | 0 | 0 | 89 | 11 | | | 75 ± 10 | 21 | 48 ± 8 | 21 | 54 ± 9 | 14 |

[a]The relative abundance of each architectural type is indicated. [b]The average dimensions (in nm) plus minus the corresponding standard deviations are indicated. *D*: diameter; *L*: length; *N*: number of measurements.

Type P: morphologies that were previously shown to be based on a regular hexameric CA lattice in which pentameric defects must be formed at certain sites (Figure S1, bottom images), leading to specific curvatures.[29] This type included open or closed quasi-spheres and teardrop-shaped or truncated cone-shaped particles, as well as (extremely infrequent) capsule-like tubes with quasi-spherical domes at the ends.

For the wt and each VLP mutant of assembly groups I or II, the relative proportion of VLPs assigned to morphology types H or P were estimated by counting the particles of each type present in many TEM fields from each of several different preparations obtained in different experiments (Table 1).

For the wt and the four group I mutants (disassembly rates similar to the wt), the assembly reaction yielded VLPs that were all assigned to morphology type H: either a very high proportion of long tubes and a few sheets (wt, 95% long tubes and 5% sheets; Q192A, 97% long tubes and 3% sheets), or long tubes only (E45A, S178A). E180A also formed tubes only, but these were much shorter than the wt tubes, and also very rough and irregular, which suggests the underlying hexagonal lattice could contain some defects. E180A was also the only group I mutant that assembled with a (somewhat) slower rate than the wt.

For the three group II mutants ((dis)assembly kinetics conspicuously different from the wt) the dominant VLP morphologies were quite different from the wt as predicted. For P38A most particles (72%) corresponded to flat sheets, tubes were much less abundant (28%). In spite of its different dominant morphology, P38A still belonged to type H (hexamer-only lattice). In contrast, group II mutants V165A and Q63A showed very high proportions of open or closed, teardrop- or truncated cone-shaped VLPs (Q63A 71%; V165A



https://doi.org/10.1021/acsnano.4c07948
ACS Nano 2024, 18, 27465−27478

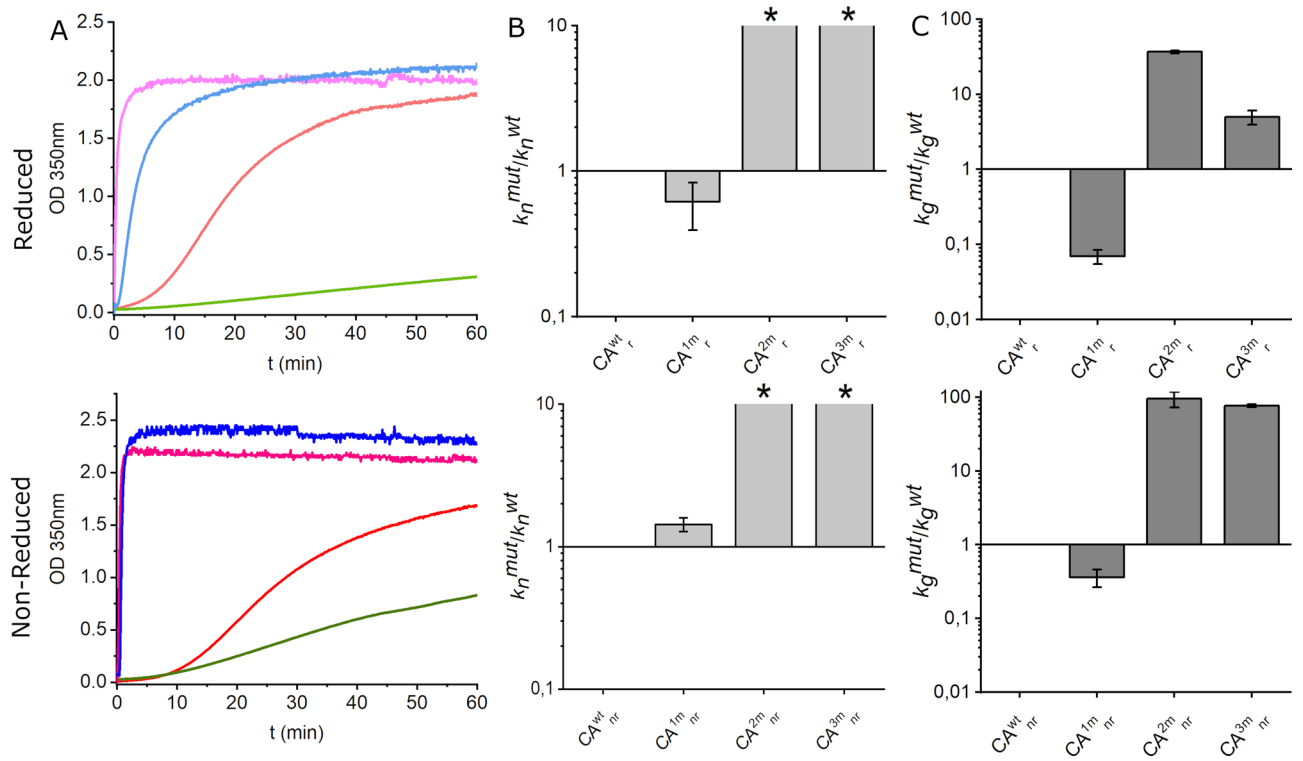



**Figure 6. Comparative self-assembly kinetics of wt and cysteine mutant CAs under reducing conditions (top graphs) or nonreducing conditions (bottom graphs). (A) Effects on the kinetics of CA self-assembly by the individual mutation of different interfacial amino acid residues to cysteine. CA polymerization was followed by monitoring the optical density (OD) at 350 nm. The curve corresponding to each variant protein in a representative experiment is color coded (top graph, reducing conditions: light red, $CA^{wt}{}_{r}$; light blue, $CA^{3m}{}_{r}$; light pink, $CA^{2m}{}_{r}$; light green, $CA^{1m}{}_{r}$; bottom graph, nonreducing conditions: red, $CA^{wt}{}_{nr}$; blue, $CA^{3m}{}_{nr}$; pink, $CA^{2m}{}_{nr}$; green, $CA^{1m}{}_{nr}$). (B) Bar plots of the ratio between the nucleation rate constant $k_n$ for each CA mutant and the $k_n$ for wt CA, averaged from data obtained in duplicate experiments ($k_n^{wt,r}$ = 0.0132 ± 0.0005 $min^{-1}$, $k_n^{wt,nr}$ = 0.0060 ± 0.0001 $min^{-1}$). For mutants $CA^{2m}$ and $CA^{3m}$, a minimum value is given (indicated by an asterisk), as the nucleation rate was faster than the experimental dead time. (C) Bar plot of the ratio between the growth rate constant $k_g$ for each CA mutant and the $k_g$ for wt CA, averaged from data obtained in duplicate experiments ($k_g^{wt,r}$ = 0.0683 ± 0.0002 OD·$min^{-1}$, $k_g^{wt,nr}$ = 0.051 ± 0.002 OD·$min^{-1}$). Error bars in (B,C) correspond to standard deviations.**

87%), together with a much smaller proportion of quasi-spheres (Q63A 12%; V165A 5%). These two mutants could, thus, be assigned to morphology type P, which require the insertion of pentameric defects to account for their particular shapes. For these two mutants, only a minor proportion of tubes were observed (Q63A 17%; V165A 8%) and, moreover, these tubes were much shorter than the wt tubes.

The approximate sizes of many individual VLPs with different morphologies were determined from TEM images, and the results were separately averaged for the wt and each mutant. The average dimensional parameters and standard deviations are indicated in Table 1. The tubes observed in stained preparations for the wt CA and each mutant (except E180A), irrespective of length, were on average 48−59 nm in diameter. These values are similar to those of assembled CA tubes (~45−50 nm in stained TEM images),[28,44] whose molecular architecture was determined at high-resolution by cryo-EM or other high-resolution techniques, and shown to be based on a regular hexameric CA lattice.[45−48] In contrast, the short, rough, and irregular E180A tubes were somewhat thinner (~41 nm average diameter).

The dimensions of VLPs showing type P morphologies were also rather uniform within and between mutants. The average diameter of quasi-spherical VLPs was 60−65 nm. The average maximum width of teardrop- or truncated cone-shaped VLPs was 68 nm, and their average length was 110−120 nm. These dimensions are very similar to those of cone-shaped authentic mature HIV-1 capsids (~60 × 120 nm), whose high-resolution molecular architecture revealed a hexameric CA lattice in which pentameric defects must be present at certain locations.[49]

**Introduction of Cysteines and Interprotein Disulfide Bridges at Interfaces in the CA Lattice.** The 7 alanine mutants described above were analyzed to determine changes in VLP assembly, disassembly, and architecture upon removal of interprotein interactions in the CA lattice. Changes in VLP morphology had previously been observed also when disulfide bonds between CA subunits were introduced through mutation of specific residues to cysteine (e.g., mutants A204C[36] or A14C/E45C.[48] It was, however, unclear whether the observed effects on assembly were due to the disulfide bonds themselves, or just to the introduced cysteines.

To differentiate between the effect on VLP assembly and morphology of introduced cysteines and that of the disulfide bridges, we used three CA mutants we had previously constructed to engineer a disulfide-linked two-dimensional protein lattice of increased mechanical robustness.[50] These three cysteine CA variants are the single mutant $CA^{1m}$ (E180C at the CTD−CTD interface); the double mutant $CA^{2m}$ (A14C/E45C at the NTD−NTD interface); and the triple mutant $CA^{3m}$ (A14C/E45C/E180C) that combines the $CA^{1m}$ and $CA^{2m}$ mutations.[50] Under nonreducing conditions, our


https://doi.org/10.1021/acsnano.4c07948
ACS Nano 2024, 18, 27465−27478

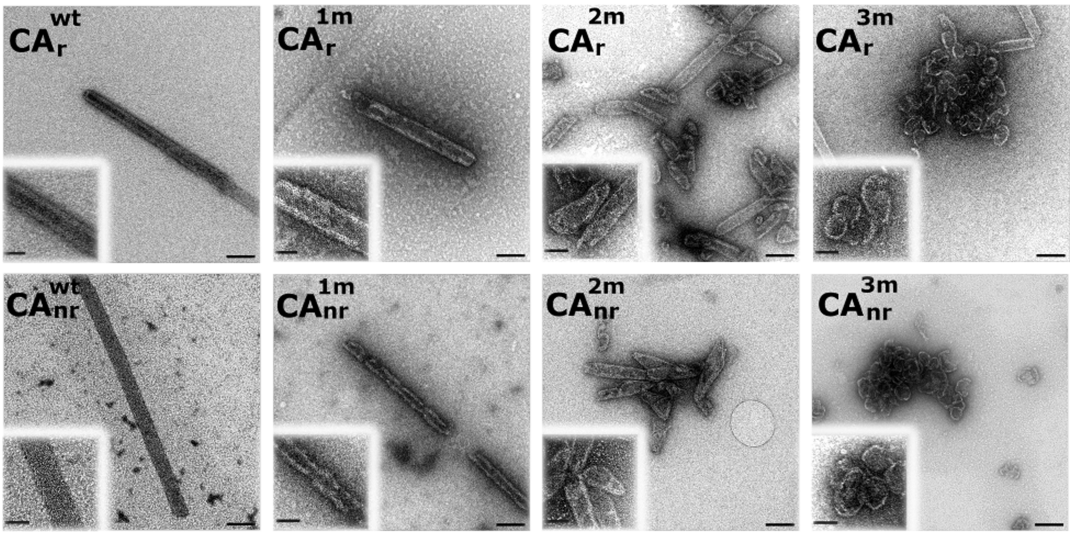



**Figure 7. Visualization by TEM of wt and cysteine mutant VLPs self-assembled *in vitro* under reducing or nonreducing conditions. The scale bars represent a length of 100 nm. The scale bars in the insets represent 50 nm.**

previous biochemical analysis confirmed that, in the $CA^{1m}$ lattice, hexamers can be covalently linked to neighbor hexamers by disulfide bridges; in the $CA^{2m}$ lattice, the monomers within each hexamer can be covalently linked by disulfide bridges; in the $CA^{3m}$ lattice, both the monomers in each hexamer and the hexamers in the lattice can be covalently linked by disulfide bridges.[50]

Those three mutants were then analyzed for assembly and morphology of the VLPs formed in solution, both under reducing (r) conditions (no disulfides formed) and nonreducing (nr) conditions (disulfides formed), as described next.

**Changes in VLP Assembly Kinetics by Introducing Cysteine Substitutions and Disulfide Bridges at Interfaces in the CA Lattice.** Assembly of the control wt VLPs and each cysteine mutant VLPs (Figure 6) was done exactly as described above for wt and the alanine mutant VLPs, but this time using both reducing conditions (Figure 6, top) and nonreducing conditions (Figure 6, bottom). The results of a representative experiment are shown in Figure 6A. For each tested VLP, the values for $k_n$ and $k_g$ were obtained in duplicate experiments, normalized relative to the wt values, and averaged. Average relative $k_n$ values and associated errors are shown in Figure 6B. Average relative $k_g$ values and associated errors are shown in Figure 6C. It was not possible to precisely determine the nucleation rate constant for the $CA^{2m}$ and $CA^{3m}$ mutants, because the nucleation reaction was faster than the experimental dead time. However, the data did reveal that for these two mutants the $k_n$ was at least 1 order of magnitude higher than the wt, both under reducing and nonreducing conditions.

The results obtained under reducing conditions (no disulfides) (Figure 6, top graphs) showed that $CA^{2m}$ both nucleated and grew much faster than wt CA ($k_g$ 36.6× the wt) whereas $CA^{1m}$ nucleated at a rate similar to the wt and grew much more slowly than the wt ($k_g$ 0.06× the wt). $CA^{3m}$ (which contains the two mutations introduced in $CA^{2m}$ plus the one introduced in $CA^{1m}$) showed an intermediate growth rate compared to $CA^{2m}$ and $CA^{1m}$ ($k_g$ 5× the wt), indicating an additive effect of the combined mutations on the assembly process (Figure 6B,C). Thus, replacement of certain interfacial amino acid residues by cysteine, like the removal of certain interfacial interactions by alanine mutations, led to substantial effects in the kinetics of VLP assembly, even in the absence of disulfide bonds.

Comparison of the results obtained under nonreducing conditions (disulfides formed) (Figure 6, bottom graphs) with those obtained under reducing conditions (no disulfides) (Figure 6, top graphs) showed that the covalent links established between the assembling CA subunits increased the growth rate. The growth rate of $CA^{1m}$ increased by 3.9× (interhexamer disulfides); that of $CA^{2m}$ by 1.9x×(intrahexamer disulfides); and that of $CA^{3m}$ by 11.7×, revealing that the interhexamer and intrahexamer disulfides combined exerted an additive or weakly cooperative effect on the assembly rate.

**Changes in VLP Architecture by Introducing Cysteine Mutations and Disulfide Bridges at Interfaces in the CA Lattice.** The morphologies and dimensions of wt CA and mutant $CA^{1m}$, $CA^{2m}$, and $CA^{3m}$ VLPs were then determined as described above for the alanine mutant VLPs (Figure 7). The cysteine mutant VLPs also showed different morphologies or mixtures of different morphologies, depending on the mutant (Figure 7). For the wt and each mutant VLP, the relative proportion of particles assigned to morphology types H or P were estimated by counting the particles of each type present in many TEM fields from each of several different preparations obtained in different experiments (Table 1).

For $CA^{1m}$ (E180C), as for the corresponding alanine mutant E180A (see above), the assembly reaction yielded only short, irregular tubes, both under reducing and nonreducing conditions. $CA^{2m}$ formed open or closed, teardrop- or truncated cone-shaped VLPs (75% or 83% of the total VLPs formed under reducing or nonreducing conditions, respectively), or quasi-spheres (12% or 9%, respectively). Only a minor proportion of tubes (13% or 8%) were observed and, again, these tubes were much shorter than the wt tubes. $CA^{3m}$ under nonreducing conditions yielded open or closed, teardrop- or truncated cone-shaped VLPs (50%) or quasi-spheres (13%), and 37% (long) tubes, a behavior that was again intermediate between those of the wt and $CA^{1m}$ on one side, and that of $CA^{2m}$ on the other. However, $CA^{3m}$ under


https://doi.org/10.1021/acsnano.4c07948
ACS Nano 2024, 18, 27465−27478

nonreducing conditions yielded 89% truncated cones and 11% quasi-spheres; no tubes were observed at all (Table 1).

The above results revealed that the replacement of A14 and E45 by cysteines, but not the replacement of E180 by cysteine, favored the formation of type P morphologies, even in the absence of disulfide bonds. The disulfides formed in $CA^{1m}$ or $CA^{2m}$ had no discernible effect on the different morphological types obtained in each case or their relative abundance. The combination of the $CA^{1m}$ and $CA^{2m}$ disulfides in $CA^{3m}$ did result in both a decrease in the proportion of tubes from 37% to 0%, and a corresponding increase in the proportion of type P, cone-shaped particles from 47% to 89% (Table 1).

The approximate sizes of many stained individual $CA^{1m}$, $CA^{2m}$, or $CA^{3m}$ VLPs with different morphologies were determined from TEM images and separately averaged (Table 1), as was done for the alanine mutants. The tubes observed for each mutant, irrespective of length, were 49−57 nm in average diameter. The dimensions of the type P morphologies were also rather uniform between and among mutants. The average diameter of quasi-spherical VLPs was 50−54 nm. The average maximum width of teardrop- or truncated cone-like VLPs was 45−53 nm, and their average length was 74−85 nm, values similar to those found for the different particle types formed by wt CA and the alanine mutants.

To sum up, different individual amino acid replacements by alanine or cysteine at protein−protein interfaces in the HIV-1 CA lattice influenced VLP assembly and/or disassembly kinetics and either favored or disfavored different assembly pathways leading to different VLP architectures. In addition, disulfide bridges within and/or between CA hexamers accelerated CA assembly, and when both bridge types were present together, they also influenced the assembly pathway. Certain amino acid substitutions at the CA−CA interfaces, or the establishment of a network of CA−CA covalent bonds, strongly favored *in vitro* the assembly of truncated cone-shaped VLPs resembling authentic mature HIV-1 capsids.

**ToD Destabilization May Determine the Different Propensity of Variant HIV-1 CAs to Assemble into Tubes or Capsid-Like Cone-Shaped Particles.** The above results revealed that, under CA assembly promoting conditions *in vitro*, certain amino acid substitutions at protein−protein interfaces in the CA lattice have no influence on VLP architecture: like wt CA, some tested CA mutants (e.g., S178A) formed long tubes whose assembly does not require the insertion of pentagonal defects in the hexagonal protein lattice (type H morphologies). However, for some other CA mutants, a dramatic change occurred in the favored assembly pathway, leading to the production of a vast majority of teardrop- or truncated cone-shaped VLPs instead of tubes. Formation of cone-shaped particles have previously been shown to require the presence of CA pentamers at certain positions in the CA protein lattice (type P morphologies). Of particular interest were CA mutants Q63A and V165A, in which certain interprotein interactions at the NTD−CTD intrahexamer interfaces had been specifically removed.

Our working hypothesis (justified in the Introduction and in Figure 2B) was that CA mutations that decrease the stability of the ToD assembly intermediate would facilitate the formation of pentagonal defects in the growing hexagonal lattice. These variants would show an increased propensity to form type P architectures (teardrop- or cone-shaped particles). Conversely, CA variants with mutations that do not significantly influence ToD stability would predominantly form, like wt CA, type H architectures (hexamer-only tubes).

The unmodified ToD intermediate is transient and cannot be isolated to experimentally test the above hypothesis. Instead, in this study, all-atom MD simulations were performed to assess the effects of some CA mutations on ToD conformation and equilibrium dynamics, on the strength of protein−protein interactions within the ToD, and on ToD stability (Figure 8 and Movie 1). Four CA variants were chosen as representatives of the ensemble of the 11 variants tested in this study for VLP assembly, disassembly, and morphology (Figure 8A). Two of the chosen CA variants (wt and S178A) assembled into hexamer-only tubes (type H morphology). The two other chosen CA variants (V165A and Q63A) assembled into teardrop- or cone-shaped particles that must include pentameric defects in the protein lattice (type P morphology).

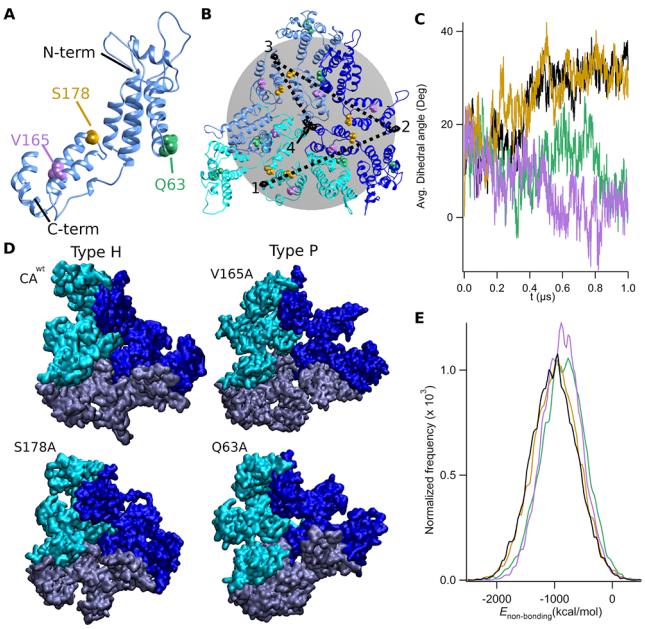



**Figure 8. Conformational dynamics and equilibrium conformation of type H and type P variants during free all-atom MD simulations. (A) Ribbon structure of the CA monomer showing residues Q63, V165, and S178 that were individually replaced by alanine residues in the corresponding CA mutants. The NTD (deep blue) and CTD (light blue) are indicated. (B) Top view of a ToD in which a dihedral angle is defined (black dotted line) between residues A204 located at the outer edge of the ToD (1 to 3) and a fourth A204 residue (4), one of the three A204 residues located very close to the center of the ToD. The gray circle delineates the plane subtended by the three A204 residues at the outer edge of the ToD. Each CA dimer within the ToD is differentially colored (cyan, deep blue, or light blue). (C) Time evolution of the averaged dihedral angles show convergence of type H CA variants (wt, black; S178A, orange) on one side and of type P CA variants (Q63A, green; V165A, purple) on the other. (D) surface representation of the equilibrium conformation of ToDs from type H variants (wt and S178A, left) or from type P variants (V165A and Q63A, right). Each dimer within the ToD is differentially color-coded, as in panel (B). (E) normalized histogram of the nonbonding (VdW and electrostatic) energy of a dimer for type P variants (Q63A, green; V165A, purple) and for type H variants (wt, black; S178A, orange).**



https://doi.org/10.1021/acsnano.4c07948
ACS Nano 2024, 18, 27465−27478

The ToD structures for each of the four chosen CA variants (Figure 8B) were computationally extracted from the non-mutated CA lattice atomic structure (PDB ID: 4xfx).[46] The corresponding mutations (S178A, V165A, or Q63A) were then virtually introduced in the ToD structure (see Methods).

Free all-atom MD simulations of 1 $\mu$s duration (see Methods) were performed with the four chosen variant ToD intermediates (Figure 8 and Movie 1). The root-mean-square deviations (rmsd) of the protein backbones remained within the 6−8 Å range in all simulations (Figure S2), which indicated that stable ToD equilibrium conformations had been reached.

Visualization of the MD trajectories showed that the ToDs corresponding to type H morphologies adopted a different equilibrium conformation with respect to the ToDs corresponding to type P morphologies. The different conformation of type P ToDs relative type H ToDs was reflected, for example, in the degree of convexity of the ToD. To support the observation that ToD equilibrium conformations segregated according to types H or P, the dihedral angle formed by the $C_\alpha$ of residues A204 (Figure 8B) was determined as a parameter to quantify ToD convexity. The temporal evolution of the dihedral angle thus calculated clearly differentiated between type H ToD variants (wt and S178A), which were more convex, and type P ToD variants (Q63A and V165A), which were flattened (Figure 8C).

Type P ToDs showed relatively large openings between the dimeric subunits (Figure 8D and Movie 1) that were not observed in type H ToDs. This observation suggested that type P ToDs are destabilized relative to type H ToDs. We estimated the interaction energy between a dimer within the ToD with the rest of the protein complex using NAMD[51] (see Methods). The association energy values were lower (more negative) for type H ToDs than for type P ToDs (Figure 8E), which directly indicates that type P ToDs are destabilized relative to type H ToDs.

To sum up, all-atom MD simulations indicate that ToDs formed by Q63A or V165A variants with increased propensity for assembly into pentamer-containing, cone-shaped particles adopt a different equilibrium conformation and are destabilized relative to ToDs formed by wt or S178A variants that assemble into hexamer-only tubes. These results are consistent with the hypothesis under test.

**A Mechanism for ToD Destabilization.** We then checked which CA−CA interactions could be removed in the ToD intermediate by type P mutations (Q63A and V165A), but not by type H mutations (S178A), which could lead to its destabilization. Analysis of interactions in the conformation a ToD adopts within the structure of an already assembled CA lattice was not considered adequate because: (i) the free ToD intermediate in solution may adopt, at equilibrium, a conformation that significantly differs from that in the assembled lattice; accordingly, high rmsd values were obtained from MD simulations when the starting ToD structure and the final, equilibrium conformations were compared (Figure 8). (ii) Beyond the removal of an atomic group, the type H and type P mutations altered the predicted ToD equilibrium conformation in different ways, again as indicated by the results of MD simulations; (iii) Like many other proteins and protein complexes, the ToD may sample different conformations around the minimum free energy conformation at equilibrium. Such different conformations were observed during the last 250 ns of the MD simulations, in which the wt and mutant ToDs had already reached equilibrium (as indicated by rmsd values and dihedral angles; Figures S2 and 8).

Instead of relying on a static picture of the ToD as a part of the assembled lattice, PyContact[52] was used to analyze the different conformations of the free ToD that fluctuated around the minimum free energy conformation at equilibrium in the last 250 ns of the MD trajectories. Pairs of residues involved in CA−CA contacts were identified for each fluctuating conformation of the wt, S178A, Q63A, or V165A ToD variants. A cutoff distance of 5 Å was chosen to include medium-range ionic interactions, as well as closer atom−atom contacts. Quantitative criteria (described in Methods) were used to evaluate the frequency of each observed CA−CA contact in the ensemble of wt and mutant ToD conformations at equilibrium (last 250 ns of the MD trajectories). The individual contacts were categorized as similarly represented, under-represented, or over-represented in a mutant ToD ensemble at equilibrium, relative to the wt ToD ensemble.

The results of the comparative analysis (Figure S3) revealed some CA−CA contacts that were frequently present in type H ToDs (wt and S178A) but not in type P ToDs (Q63A and V165A). These type H characteristic contacts were located at CTD−CTD interfaces, close to the 3-fold axis at the ToD center. In addition, some CA−CA contacts that were not frequently present in type H ToDs occurred in type P ToDs. These type P characteristic contacts were located at NTD−NTD interfaces close to the ToD edge. Moreover, visual inspection of individual conformations along the MD trajectories clearly revealed conspicuous differences in the local conformation around the different CA−CA interfaces. Thus, destabilization of the ToD by type P mutations appears to arise from (i) significant distortions of CA−CA interfaces, and (ii) a reduced interaction energy in the CTD−CTD interface in each CA dimer within the ToD intermediate. The higher propensity for dissociation of the CA monomers in the CA dimer could facilitate the dissociation of a dimer from a ToD as proposed (Figure 2B), though not as a single unit. The debilitated CTD−CTD interface would instead facilitate the successive release of the two monomer subunits of the same dimer in the ToD.

CA residues Q63 and V165 are located at CTD−NTD interfaces (Figure 1), so it may come as a surprise that they are predicted to distort the CTD−CTD interfaces in the ToD. In fact, an analogous situation was previously observed on binding the peptide CAI to CA. CAI binds a site in CA that is very close to the Q63 and V165 residues at the CTD−NTD interface, but the bound peptide actually distorted the CTD−CTD interface, reduced the strength of the CTD−CTD interaction in each CA dimer, and impaired VLP assembly.[53] In addition, mutation to alanine of residue Y169, located not far from V165, also distorted the CTD−CTD interface like the CAI peptide did.[54]

We have no evidence yet to indicate that the cysteine mutations in $CA^{2m}$ and $CA^{3m}$, or the disulfide bonds in $CA^{3m}$, favor the production of cone-shaped VLPs by destabilizing the ToD intermediate in the same way that the Q63A and V165A mutations do. In principle, the cysteine residues introduced in $CA^{2m}$ could destabilize the ToD by removing some CA−CA interactions, introducing steric clashes, or distorting the protein−protein interfaces. In turn, the combination of NTD−NTD and CTD-CTD disulfides in $CA^{3m}$ could reduce ToD stability because of the need to satisfy severe steric constraints through an energetically unfavorable conforma-


https://doi.org/10.1021/acsnano.4c07948
ACS Nano 2024, 18, 27465−27478

tional rearrangement of CA. The disulfide network in $CA^{3m}$ could also lead to an increase in the association free energy by reducing the conformational entropy of the system; such a reduction could not be fully compensated by a reduction in enthalpy due to the formation of the disulfide bonds. In contrast, when only one or the other disulfide types was introduced separately in $CA^{1m}$ and $CA^{2m}$ under nonreducing conditions, less steric constraints would occur, and the ToD would not be destabilized. Further studies are required to assess whether mechanisms other than ToD destabilization may promote the formation of cone-shaped VLPs *in vitro*.

**ToD Instability as a Determinant for the Formation of Pentamer Defects During Capsid Assembly in the Maturing HIV-1 Virion?** The typical outcome of many attempts for achieving *in vitro* the self-assembly of free CA from HIV-1 into pentamer-containing, cone-shaped VLPs resembling authentic capsids was the formation of hexamer-only tubes instead. This result underscores the need for a better understanding of the structural determinants of protein self-assembly, if one wishes to devise effective bottom-up approaches to fabricate protein-based nanoparticles of defined size and architecture for specific uses.

In principle, one could guess that a cone-shaped HIV-1 capsid could be assembled through the association of CA monomers and dimers into relatively stable hexameric and pentameric intermediates and that certain conditions could favor the insertion of a pentamer between hexamers during their association to form the capsid. However, to our knowledge, no evidence supports the assembly of the mature HIV-1 capsid from a mixture of hexameric and pentameric building blocks or intermediates. Instead, the available evidence regarding self-assembly of HIV-1 CA favors a ToD[38] as a dominant intermediate in a nucleation and growth pathway to form higher-order nanostructures.

The necessity of including pentamers in the lattice to build an authentic HIV-1 capsid calls for a complex scenario in which, in addition to ToDs, CA monomers and other CA oligomers may also join the growing CA lattice[38] or dissociate from it. Consistent with this idea, visualization in real time of the growth of a two-dimensional hexameric HIV-1 CA lattice *in vitro* using high-speed atomic force microscopy revealed a reversible, stochastic association and dissociation of CA monomers and different types of CA oligomers to the growing protein lattice.[55]

In the model by Tsiang et al.,[38] a pentamer can be formed in the growing CA lattice by sharing a dimer between two neighbor ToDs (Figure 2A). We envisaged that this situation could be achieved during capsid assembly by association of one DoD with two ToDs (Figure 2B). Transient DoDs could result from the dissociation of a dimer from a ToD (or, rather, as indicated by the above results, the stepwise dissociation of the two monomers of a dimer). DoDs may also transiently appear during the stepwise association of CA dimers to form a ToD. The results obtained in the present study suggest that conditions required for CA self-assembly *in vitro* (a high ionic strength that screen CA-CA repulsions[30,31]) may also stabilize the ToD intermediate. As a consequence of ToD stabilization, the DoD population would be smaller, which would decrease the probability of the formation of pentameric defects in the VLPs being assembled. The stepwise addition of ToDs only to an assembly nucleus would result in the formation of a purely hexagonal CA lattice without pentameric defects, giving rise to tubes (or sheets), as typically observed for the wild-type CA *in vitro*. To achieve the formation of cone-shaped VLPs instead of tubular VLPs, the stability of the ToD intermediate may have to be maintained below a certain threshold. Such a requirement was fulfilled under *in vitro* assembly conditions (high ionic strength) through the introduction of certain CA mutations (e.g., Q63A or V165A) that would reduce the strength of CA-CA interactions in the ToD. The destabilization of the ToD would increase the DoD population and, thus, the probability of formation of pentameric defects to yield cone-shaped VLPs *in vitro*.

The results of the present study suggest the possibility that, under the conditions found inside the virion, the ToD intermediate formed by wild-type CA may not be as stable as at the very high ionic strength and unconfined environment found during CA assembly *in vitro*. A low ToD stability may contribute to some extent to the formation of pentamers inside the virus particle, favoring the assembly of a cone-shaped capsid.

However, it should be emphasized that closed, cone-shaped particles resembling authentic HIV-1 capsids were not the only pentamer-containing particles formed by the type P CA mutants *in vitro*; open teardrop-shaped particles and closed or open spheres were also formed in sizable proportions. Thus, type P mutations in CA and their ToD-destabilizing effect were not enough to direct the inclusion of pentamers exclusively to some specific positions in the CA lattice. In contrast, in the virion, nonmutated CA assembles into closed cone-shaped capsids almost exclusively (although aberrant open particles are sometimes found[56]). Theory and/or experiment indicates that several factors inside the virion may promote the inclusion of pentamers at defined positions in the lattice to efficiently yield cone-shaped capsids. These factors include: the confined space within the MA shell, that may affect the curvature of the growing CA lattice;[33,56] the presence of the lipid envelope, MA shell and NC/RNA complex that may electrostatically interact with the CA subunits and even act as a template;[33,57] the interaction of other viral or cellular molecules (like IP6 or CypA) enclosed in the virion;[58,59] etc. Coarse-grained molecular dynamics simulations indicate that the radius of spontaneous curvature for a conical capsid is different than that for a cylindrical particle. Inside the virion, the growing CA lattice may curl into the shape of a cone,[56,60] and the inclusion of pentamers at quite specific positions would be unavoidable to relieve the accumulated stress.[61]

## CONCLUSIONS

The evidence obtained in this study supports the hypothesis that the stability of a major, transient assembly intermediate (a trimer of CA dimers, ToD) may control the HIV-1 capsid self-assembly pathway, leading to the formation of nanoparticles with different architectures. If the ToD becomes very stable, for example under conditions required for CA polymerization *in vitro* (high ionic strength), tubular nanoparticles will be formed. If the ToD stability is kept relatively low, for example, by introducing mutations in CA that compensate for the stabilization of the ToD under *in vitro* assembly conditions, cone-shaped nanoparticles resembling authentic HIV-1 capsids will be formed. The dependence on ToD stability of the HIV-1 capsid assembly pathway may be explained by the following model. Dimers of CA dimers (DoDs) in addition to ToDs may be required for the formation of pentamers during growth of the protein lattice. DoDs would transiently occur as intermediates during ToD oligomerization, and/or as a


https://doi.org/10.1021/acsnano.4c07948
ACS Nano 2024, 18, 27465−27478

consequence of the dissociation of a dimer from a ToD. ToD stabilization would reduce the DoD population, increasing the frequency of hexamer-only tubes. ToD destabilization would increase the DoD population, increasing the frequency of pentamer-containing cone-shaped particles.

## METHODS

**Mutagenesis, Protein Expression and Purification.** Mutations were introduced in a recombinant plasmid coding for CA from HIV-1 (strain BH10)[32] using the Quick Change II site-directed mutagenesis Kit (Stratagene). The presence of the desired mutations and absence of other mutations was confirmed by nucleotide sequencing. The CA protein was expressed in *E. coli* BL21(DE3) cells that had been transfected with a recombinant plasmid pET21b(+) containing the coding sequence for wt CA or the chosen CA mutants, and purified as previously described.[32] In brief, cell cultures were grown at 37 °C and protein expression was induced by the addition of 1 mM IPTG and incubation for 3 h. Cells were harvested and frozen at −20 °C for storage. The cells were thawed and resuspended in 50 mM Tris-HCl pH = 8 containing 5 mM $\beta$-mercaptoethanol for wt CA and alanine mutants and in 50 mM Tris-HCl pH = 8 containing 20 mM DTT for the cysteine mutants and lysed by sonication. After centrifugation, CA protein in the soluble fraction was purified by ammonium sulfate fractionation, ion exchange chromatography in SP-Sepharose, and size-exclusion chromatography in a Superdex 75 (Amersham Biotech). The solution of purified CA thus obtained was thoroughly dialyzed against phosphate buffered saline (PBS) for wt CA and alanine mutants and against PBS containing 20 mM DTT for the cysteine mutants and stored at −80 °C until use. Protein purity was assessed by polyacrylamide gel electrophoresis. The concentration of CA protein stocks was determined by UV spectrophotometry.

**Self-Assembly of Wt and Mutant CAs *In Vitro* and Kinetic Analysis.** Assembly reactions were performed as previously described[31] with some modifications. The reaction mixtures were incubated at room temperature (23 °C) and a CA concentration of 38 $\mu$M in PBS pH 7.4 for the alanine mutants and the wt control; or, alternatively, in PBS pH 7.4 containing 4 mM DTT (reducing conditions) or 10 mM cystamine (nonreducing conditions) for the cysteine mutants and the wt control. The assembly reaction was triggered by adding NaCl to a final concentration of 2.25 M. The OD at 350 nm was determined as a function of time to monitor the appearance of high order structures using a Shimadzu UV-1603 spectrophotometer. The time-dependent increase in OD was fitted to a sigmoidal function based on the F−W two step model:[43]

$$OD_t = A_0 - A_0\left(\frac{k_n + k_g A_0}{k_g A_0 + k_n e^{(k_n + k_g A_0)t}}\right) \quad (1)$$

where $OD_t$ is the optical density at 350 nm and time $t$, $A_0$ represents the initial light scattering of the initial free CA, $k_n$ is the nucleation rate and $k_g$ is the growth rate. Maximum rates were calculated from the first derivative of eq 1.

**Disassembly of CA Protein Wild-Type and Mutant Proteins *In Vitro* and Kinetic Analysis.** CA VLPs previously assembled as described above and kept at room temperature (23 °C) were diluted 10-fold in the same reaction buffer to trigger their disassembly.[42] The OD at 350 nm was determined as a function of time to monitor the disappearance of high order structures using a Shimadzu UV-1603 spectrophotometer. The time-dependent decrease in OD was fitted to a single-exponential function:

$$OD_t = OD_f + A \cdot e^{-k_d t} \quad (2)$$

where $OD_t$ is the optical density at time $t$, $A$ is the pre-exponential factor, $k_d$ is the dissociation rate constant, and $OD_f$ is the optical density at infinite time.

**Negative Staining and Visualization of VLPs by TEM.** The CA assembly products were used undiluted for wt CA, P38A, E45A, Q63A, S178A, Q192A, E180A, and $CA^{1m}$, and diluted 1/10 in reaction buffer for V165A, $CA^{2m}$, and $CA^{3m}$ to reduce the VLP concentration in the samples. The diluted $CA^{3m}{}_{nr}$ products were sonicated 10 s to help disperse the VLPs present in the samples. Eight $\mu$L aliquots were deposited on ionized Formvar/carbon-coated copper grids. The samples were fixed for 2 min, washed twice with distilled water, negatively stained with 2% (wt/vol) uranyl acetate for 60 s, dried, and visualized in JEM-1010 or JEM-1400 (JEOL) electron microscopes at magnifications of ×60,000 or ×80,000. The dimensions of many individual VLPs of different types were estimated from TEM images. The number of individual VLPs measured in each case is indicated in Table 1. For tubular VLPs, the external diameter was measured. For the truncated cone- or teardrop-shaped VLPs length, the length along the long axis and the maximum width ($\Phi_{max}$) were measured. For quasi-spherical VLPs, the diameter along two perpendicular axes were measured.

**All-Atom MD Simulations.** The atomic structure of a CA monomer in a hexagonal CA crystal (PDB ID: 4xfx) was used as a starting model. Missing residues were added using Modeller.[62] Then, transformation matrices were applied to construct a small patch of the flat hexagonal CA lattice. Protonation states were calculated with the H++ server[63] A ToD atomic model was extracted from the flat lattice and fed to the Leap module of AmberTools[64] to add protons and the intrachain disulfide bond (Cys198-Cys218) using the force field ff14SB.[65] Models for the three ToD mutants (Q63A, V165A, and S178A) were obtained by replacing the corresponding amino acid residues with alanine in the previously constructed wt ToD model. Models were solvated using TIP3P water molecules,[66] including $Na^+$ and $Cl^-$ ions to neutralize the system and reach 150 mM NaCl.[67]

The systems were simulated with OpenMM[68] with a time step of 2 fs. The integrator used was a Langevin Middle Integrator at 298 K with a collision rate of 1.0 $ps^{-1}$. Nonbonding interactions were treated by particle mesh−Ewald with a nonbonding cutoff of 8 Å and hydrogen bond length was restricted. Pressure was kept constant to 1 bar via Monte Carlo Barostat. Periodic boundary conditions in combination with a flat-bottom potential (force constant of 5.0 kcal·$mol^{-1}$·$Å^{-2}$) were implemented to keep the system within the simulation box. The systems were minimized with default parameters and thermally equilibrated to 298 K. Free molecular dynamics was run for 1 $\mu$s in the production phase.

Trajectories were processed and analyzed with cpptraj[69] and VMD.[70] The GetContacts library was used to quantify VdW interactions and the NAMD Energy Plugging of VMD, was used to evaluate nonbonding energy contributions using NAMD.[51]

To evaluate the specific contacts assigned to type H or P architectures PyContact[52] was used. First, frequency contact


https://doi.org/10.1021/acsnano.4c07948
ACS Nano 2024, 18, 27465−27478

matrices for wt CA and the three chosen mutant proteins were obtained via the "ContactFrequency" method. As the residue indices in the MD topology file are sequential, residue indices for the contacts were mapped to the equivalent residue indices in the monomer (1−231). To remove redundant contacts after mapping, only the highest frequency for each monomer residue index pair was preserved. After obtaining the difference in frequency between each contact in the mutant and the equivalent contact in wt CA, those presenting a difference greater than 0.5 were considered over-represented; those showing a difference lower than −0.5 were considered under-represented; and those with a difference in the range 0.25 to −0.25 were considered similarly represented in both the mutant and the wt. Those contacts tagged as over-represented for V165A and Q63 and similarly represented for S178A were considered as characteristic of type P ToD conformations at equilibrium (last 250 ns of the MD simulations); those contacts tagged as under-represented for V165A and Q63 and similarly represented for S178A were considered as characteristic of type H ToD conformations at equilibrium.

## ASSOCIATED CONTENT

### Data Availability Statement

The data that support the findings of this study are available from the corresponding authors upon reasonable request.

### Supporting Information

The Supporting Information is available free of charge at https://pubs.acs.org/doi/10.1021/acsnano.4c07948.

Interactions in HIV-1 tubular VLPs and conservation of CA residues chosen for mutational analysis; representative type H and type P VLPs; rmsd values between atomic positions in ToD structures along a MD simulation and the starting ToD conformation; residues with a role in type H and type P ToDs (PDF)

Surface representation of type H (wt and S178A) and type P (Q63A and V165A) ToD conformations along MD simulations (MP4)

## AUTHOR INFORMATION


### Corresponding Authors

**Alejandro Valbuena** − *Virus Engineering Group, Centro de Biología Molecular Severo Ochoa (CSIC-UAM), Madrid 28049, Spain*; Email: avalbuena@cbm.csic.es

**Mauricio G. Mateu** − *Virus Engineering Group, Centro de Biología Molecular Severo Ochoa (CSIC-UAM), Madrid 28049, Spain*; orcid.org/0000-0002-2915-1529; Email: mgarcia@cbm.csic.es

### Authors

**Judith Escrig** − *Virus Engineering Group, Centro de Biología Molecular Severo Ochoa (CSIC-UAM), Madrid 28049, Spain*

**íñigo Marcos-Alcalde** − *Molecular Modeling Group, Centro de Biología Molecular Severo Ochoa (CSIC-UAM), Madrid 28049, Spain*; orcid.org/0000-0002-0674-6423

**Santos Domínguez-Zotes** − *Virus Engineering Group, Centro de Biología Molecular Severo Ochoa (CSIC-UAM), Madrid 28049, Spain*; Present Address: mAbxience (Genhelix), Julia Morros s/n, 24009 Armunia, León, Spain

**David Abia** − *Bioinformatics Unit, Centro de Biología Molecular Severo Ochoa (CSIC-UAM), Campus of the Universidad Autónoma de Madrid, Madrid 28049, Spain*

**Paulino Gómez-Puertas** − *Molecular Modeling Group, Centro de Biología Molecular Severo Ochoa (CSIC-UAM), Madrid 28049, Spain*; orcid.org/0000-0003-3131-729X

Complete contact information is available at: https://pubs.acs.org/10.1021/acsnano.4c07948


### Author Contributions

J.E. performed the experiments and analyzed data. S.D.-Z. provided some biological material and performed some auxiliary experiments. A.V. devised an interpretative model based on ToD stability and designed MD simulations. I.M-A. and D.A. performed simulations. A.V., M.G.M., and P.G.-P. interpreted results. M.G.M. and A.V. designed the study and wrote the paper.

### Notes

The authors declare no competing financial interest.

## ACKNOWLEDGMENTS

This work was funded by grants to M.G.M. (MICINN/FEDER EU RTI2018-096635-B-I00 and PID2021-126973OB-I00) and to P.G.-P (MCIU-AEI RTI2018-094434-B-I00 and MICINN FEDER EU PID2021-126625OB-I00/10.13039/501100011033/), and benefitted also from institutional grants from the Severo Ochoa Program for Centers of Excellence in R&D (CEX2021-00154-S) and Fundación Ramón Areces to the Centro de Biología Molecular Severo Ochoa. M.G.M. is an associate member of the Institute for Biocomputation and Physics of Complex Systems, Zaragoza, Spain.

## REFERENCES


(1) Springer International Publishing. Protein-Based Engineered Nanostructures In *Advances in Experimental Medicine and Biology*, Cortajarena, A. L.; Grove, T. Z.; Eds., Springer International Publishing: Switzerland, 2016, Vol. *940*. .

(2) Kuan, S. L.; Bergamini, F. R. G.; Weil, T. Functional Protein Nanostructures: A Chemical Toolbox. *Chem. Soc. Rev.* **2018**, *47*, 9069−9105.

(3) Zhang, D.; Wang, Y. Functional Protein-Based Bioinspired Nanomaterials: From Coupled Proteins, Synthetic Approaches, Nanostructures to Applications. *Int. J. Mol. Sci.* **2019**, *20*, 3054.

(4) Zhang, J.-T.; Ma, J.; Kankala, R. K.; Yu, Q.; Wang, S.-B.; Chen, A.-Z. Recent Advances in Fabrication of Well-Organized Protein-Based Nanostructures. *ACS Appl. Bio Mater.* **2021**, *4*, 4039−4048.

(5) Han, S.; Jung, Y. Artificial Protein Assemblies with Well-Defined Supramolecular Protein Nanostructures. *Biochem. Soc. Trans.* **2021**, *49*, 2821−2830.

(6) Hazra, D.; Roychowdhury, A. Protein-Based Nanostructures. In *Nanomaterials in Clinical Therapeutics: Synthesis and Applications*, Mukhopadhyay, M.; Kuila, A., Eds.; Scrivener Publishing LLC, 2022; pp. 269283. .

(7) Prevelige, P. E.; Thomas, D.; King, J. Nucleation and Growth Phases in the Polymerization of Coat and Scaffolding Subunits into Icosahedral Procapsid Shells. *Biophys. J.* **1993**, *64*, 824−835.

(8) Ceres, P.; Zlotnick, A. Weak Protein−Protein Interactions Are Sufficient To Drive Assembly of Hepatitis B Virus Capsids. *Biochemistry* **2002**, *41*, 11525−11531.

(9) Johnson, J. M.; Tang, J.; Nyame, Y.; Willits, D.; Young, M. J.; Zlotnick, A. Regulating Self-Assembly of Spherical Oligomers. *Nano Lett.* **2005**, *5*, 765−770.

(10) Katen, S.; Zlotnick, A. The Thermodynamics of Virus Capsid Assembly. *Meth. Enzymol.* **2009**, *455*, 395−417.

(11) Zlotnick, A.; Fane, B. A. Mechanisms of Icosahedral Virus Assembly. In *Structural Virology*, Agbandje-McKenna, M.; McKenna, R.; Eds.; RSC Publishing: Cambridge, 2011; pp. 180202. .

(12) Mateu, M. G. Assembly. Stability and Dynamics of Virus Capsids. *Arch. Biochem. Biophys.* **2013**, *531*, 65−79.
(13) Medrano, M.; Fuertes, M. Á.; Valbuena, A.; Carrillo, P. J. P.; Rodríguez-Huete, A.; Mateu, M. G. Imaging and Quantitation of a Succession of Transient Intermediates Reveal the Reversible Self-Assembly Pathway of a Simple Icosahedral Virus Capsid. *J. Am. Chem. Soc.* **2016**, *138*, 15385−15396.
(14) Kra, K.; Li, S.; Gargowitsch, L.; Degrouard, J.; Pérez, J.; Zandi, R.; Bressanelli, S.; Tresset, G. Energetics and Kinetic Assembly Pathways of Hepatitis B Virus Capsids in the Presence of Antivirals. *ACS Nano* **2023**, *17*, 12723−12733.
(15) Panahandeh, S.; Li, S.; Dragnea, B.; Zandi, R. Virus Assembly Pathways Inside a Host Cell. *ACS Nano* **2022**, *16*, 317−327.
(16) Almendral, J. M. Assembly of Simple Icosahedral Viruses. In *Structure and Physics of Viruses*, Mateu, M. G., Eds.; Springer: Netherlands, Dordrecht, 2013; Vol. *68*; pp. 307328. .
(17) San Martín, C. Structure and Assembly of Complex Viruses. In *Structure and Physics of Viruses*, Mateu, M., Eds.; Springer: Netherlands, Dordrecht, 2013; Vol. *68*; pp. 329360. .
(18) Bancroft, J. B. The Self-Assembly of Spherical Plant Viruses. *Adv. Virus Res.* **1970**, *16* (19), 99−134.
(19) Zhou, S.; Standring, D. N. Hepatitis B Virus Capsid Particles Are Assembled From Core-Protein Dimer Precursors. *Proc. Natl. Acad. Sci. U. S. A.* **1992**, *89*, 10046−10050.
(20) Kirnbauer, R.; Booy, F.; Cheng, N.; Lowy, D. R.; Schiller, J. T. Papillomavirus Major Capsid Protein L1 Self-Assembles into Virus-Like Particles That Are Highly Immunogenic. *Proc. Natl. Acad. Sci. U. S. A.* **1992**, *89*, 12180−12184.
(21) Ehrlich, L. S.; Agresta, B. E.; Carter, C. A. Assembly of Recombinant Human Immunodeficiency Virus Type 1 Capsid Protein in Vitro. *J. Virol.* **1992**, *66*, 4874−4883.
(22) Casini, G. L.; Graham, D.; Heine, D.; Garcea, R. L.; Wu, D. T. In Vitro Papillomavirus Capsid Assembly Analyzed by Light Scattering. *Virology* **2004**, *325*, 320−327.
(23) Bajaj, S.; Banerjee, M. In Vitro Assembly of Polymorphic Virus-like Particles from the Capsid Protein of a Nodavirus. *Virology* **2016**, *496*, 106−115.
(24) Patterson, A.; Zhao, Z.; Waymire, E.; Zlotnick, A.; Bothner, B. Dynamics of Hepatitis B Virus Capsid Protein Dimer Regulate Assembly through an Allosteric Network. *ACS Chem. Biol.* **2020**, *15*, 2273−2280.
(25) Kavčič, L.; Kežar, A.; Koritnik, N.; Žnidarič, M. T.; Klobučar, T.; Vičič, Ž.; Merzel, F.; Holden, E.; Benesch, J. L. P.; Podobnik, M. From Structural Polymorphism to Structural Metamorphosis of the Coat Protein of Flexuous Filamentous Potato Virus Y. *Commun. Chem.* **2024**, *7*, 14.
(26) Mateu, M. G. A.Assembly, Engineering and Applications of Virus-Based Protein Nanoparticles*Protein-based Engineered Nanostructures*Cortajarena, A. L.; Grove, T. Z.Eds.SpringerCham2016 Vol. *940*pp. 83120.
(27) Selivanovitch, E.; Douglas, T. Virus Capsid Assembly across Different Length Scales Inspire the Development of Virus-Based Biomaterials. *Curr. Opin. Virol.* **2019**, *36*, 38−46.
(28) Perilla, J. R.; Hadden-Perilla, J. A.; Gronenborn, A. M.; Polenova, T. Integrative structural biology of HIV-1 capsid protein assemblies: Combining experiment and computation. *Curr. Opin. Virol.* **2021**, *48*, 57−64.
(29) Lanman, J.; Sexton, J.; Sakalian, M.; Prevelige, P. E., Jr. Kinetic Analysis of the Role of Intersubunit Interactions in Human Immunodeficiency Virus Type 1 Capsid Protein Assembly In Vitro. *J. Virol.* **2002**, *76*, 6900−6908.
(30) Douglas, C. C.; Thomas, D.; Lanman, J.; Prevelige, P. E. Investigation of N-Terminal Domain Charged Residues on the Assembly and Stability of HIV-1 CA. *Biochemistry* **2004**, *43*, 10435−10441.
(31) Del Álamo, M.; Mateu, M. G. Electrostatic Repulsion, Compensatory Mutations, and Long-Range Non-Additive Effects at the Dimerization Interface of the HIV Capsid Protein. *J. Mol. Biol.* **2005**, *345*, 893−906.
(32) Del Álamo, M.; Rivas, G.; Mateu, M. G. Effect of Macromolecular Crowding Agents on Human Immunodeficiency Virus Type 1 Capsid Protein Assembly In Vitro. *J. Virol.* **2005**, *79*, 14271−14281.
(33) Ning, J.; Erdemci-Tandogan, G.; Yufenyuy, E. L.; Wagner, J.; Himes, B. A.; Zhao, G.; Aiken, C.; Zandi, R.; Zhang, P. In vitro protease cleavage and computer simulations reveal the HIV-1 capsid maturation pathway. *Nat. Commun.* **2016**, *7*, 13689.
(34) Valbuena, A.; Mateu, M. G. Quantification and Modification of the Equilibrium Dynamics and Mechanics of a Viral Capsid Lattice Self-Assembled as a Protein Nanocoating. *Nanoscale* **2015**, *7*, 14953−14964.
(35) Ganser-Pornillos, B. K.; von Schwedler, U. K.; Stray, K. M.; Aiken, C.; Sundquist, W. I. Assembly Properties of the Human Immunodeficiency Virus Type 1 CA Protein. *J. Virol.* **2004**, *78*, 2545−2552.
(36) Zhao, G.; Perilla, J. R.; Yufenyuy, E. L.; Meng, X.; Chen, B.; Ning, J.; Ahn, J.; Gronenborn, A. M.; Schulten, K.; Aiken, C.; Zhang, P. Mature HIV-1 Capsid Structure by Cryo-Electron Microscopy and All-Atom Molecular Dynamics. *Nature* **2013**, *497*, 643−646.
(37) Chen, B.; Tycko, R. Simulated Self-Assembly of the HIV-1 Capsid: Protein Shape and Native Contacts Are Sufficient for Two-Dimensional Lattice Formation. *Biophys. J.* **2011**, *100*, 3035−3044.
(38) Tsiang, M.; Niedziela-Majka, A.; Hung, M.; Jin, D.; Hu, E.; Yant, S.; Samuel, D.; Liu, X.; Sakowicz, R. A Trimer of Dimers Is the Basic Building Block for Human Immunodeficiency Virus-1 Capsid Assembly. *Biochemistry* **2012**, *51*, 4416−4428.
(39) Summers, B. J.; Digianantonio, K. M.; Smaga, S. S.; Huang, P.-T.; Zhou, K.; Gerber, E. E.; Wang, W.; Xiong, Y. Modular capsid assemblies reveal diverse host-capsid recognition mechanisms. *Cell Host Microbe* **2019**, *26*, 203−216.
(40) Yufenyuy, E. L.; Aiken, C. The NTD-CTD Intersubunit Interface Plays a Critical Role in Assembly and Stabilization of the HIV-1 Capsid. *Retrovirology* **2013**, *10*, 29.
(41) Yang, R.; Shi, J.; Byeon, I.-J. L.; Ahn, J.; Sheehan, J. H.; Meiler, J.; Gronenborn, A. M.; Aiken, C. Second-Site Suppressors of HIV-1 Capsid Mutations: Restoration of Intracellular Activities without Correction of Intrinsic Capsid Stability Defects. *Retrovirology* **2012**, *9*, 30.
(42) Del Álamo, M.; Neira, J. L.; Mateu, M. G. Thermodynamic Dissection of a Low Affinity Protein-Protein Interface Involved in Human Immunodeficiency Virus Assembly. *J. Biol. Chem.* **2003**, *278*, 27923−27929.
(43) Bentea, L.; Watzky, M. A.; Finke, R. G. Sigmoidal Nucleation and Growth Curves Across Nature Fit by the Finke−Watzky Model of Slow Continuous Nucleation and Autocatalytic Growth: Explicit Formulas for the Lag and Growth Times Plus Other Key Insights. *J. Phys. Chem. C* **2017**, *121*, 5302−5312.
(44) Li, S.; Hill, C. P.; Sundquist, W. I.; Finch, J. T. Image Reconstructions of Helical Assemblies of the HIV-1 CA Protein. *Nature* **2000**, *407* (6802), 409−413.
(45) Ganser-Pornillos, B. K.; Cheng, A.; Yeager, M. Structure of Full-Length HIV-1 CA: A Model for the Mature Capsid Lattice. *Cell* **2007**, *131*, 70−79.
(46) Gres, A. T.; Kirby, K. A.; KewalRamani, V. N.; Tanner, J. J.; Pornillos, O.; Sarafianos, S. G. X-Ray Crystal Structures of Native HIV-1 Capsid Protein Reveal Conformational Variability. *Science* **2015**, *349*, 99−103.
(47) Perilla, J. R.; Zhao, G.; Lu, M.; Ning, J.; Hou, G.; Byeon, I.-J. L.; Gronenborn, A. M.; Polenova, T.; Zhang, P. CryoEM Structure Refinement by Integrating NMR Chemical Shifts with Molecular Dynamics Simulations. *J. Phys. Chem. B* **2017**, *121*, 3853−3863.
(48) Pornillos, O.; Ganser-Pornillos, B. K.; Kelly, B. N.; Hua, Y.; Whitby, F. G.; Stout, C. D.; Sundquist, W. I.; Hill, C. P.; Yeager, M. X-Ray Structures of the Hexameric Building Block of the HIV Capsid. *Cell* **2009**, *137*, 1282−1292.
(49) Bush, D. L.; Vogt, V. M. In Vitro Assembly of Retroviruses. *Annu. Rev. Virol.* **2014**, *1*, 561−580.


https://doi.org/10.1021/acsnano.4c07948
*ACS Nano* 2024, 18, 27465−27478

(50) Domínguez-Zotes, S.; Fuertes, M. A.; Rodríguez-Huete, A.; Valbuena, A.; Mateu, M. G. A Genetically Engineered, Chain Mail-Like Nanostructured Protein Material with Increased Fatigue Resistance and Enhanced Self-Healing. *Small* **2022**, *18*, 2105456.
(51) Phillips, J. C.; Braun, R.; Wang, W.; Gumbart, J.; Tajkhorshid, E.; Villa, E.; Chipot, C.; Skeel, R. D.; Kalé, L.; Schulten, K. Scalable Molecular Dynamics with NAMD. *J. Comput. Chem.* **2005**, *26*, 1781−1802.
(52) Scheurer, M.; Rodenkirch, P.; Siggel, M.; Bernardi, R. C.; Schulten, K.; Tajkhorshid, E.; Rudack, T. PyContact: Rapid, Customizable, and Visual Analysis of Noncovalent Interactions in MD Simulations. *Biophys. J.* **2018**, *114* (3), 577−583.
(53) Ternois, F.; Sticht, J.; Duquerroy, S.; Kräusslich, H.-G.; Rey, F. A. Crystal structure of the HIV-1 capsid protein C-terminal domain in complex with an inhibitor of particle assembly. *Nat. Struct. Mol. Biol.* **2005**, *12*, 678−682.
(54) Bartonova, V.; Igonet, S.; Sticht, J.; Glass, B.; Habermann, A.; Vaney, M.-C.; Sehr, P.; Lewis, J.; Rey, F. A.; Kräusslich, H.-G. Residues in the HIV-1 capsid assembly inhibitor binding site are essential for maintaining the assembly-competent quaternary structure of the capsid protein. *J. Biol. Chem.* **2008**, *283*, 32024−32033.
(55) Valbuena, A.; Maity, S.; Mateu, M. G.; Roos, W. H. Visualization of Single Molecules Building a Viral Capsid Protein Lattice through Stochastic Pathways. *ACS Nano* **2020**, *14*, 8724−8734.
(56) Yu, Z.; Dobro, M. J.; Woodward, C. L.; Levandosky, A.; Danielson, C. M.; Sandrin, V.; Shi, J.; Aiken, C.; Zandi, R.; Hope, T. J.; et al. Unclosed HIV-1 capsids suggest a curled sheet model of assembly. *J. Mol. Biol.* **2013**, *425*, 112−123.
(57) Benjamin, J.; Ganser-Pornillos, B. K.; Tivol, W. F.; Sundquist, W. I.; Jensen, G. J. Three dimensional structure of HIV-1 virus-like particles by electron cryotomography. *J. Mol. Biol.* **2005**, *346*, 577−588.
(58) Dick, R. A.; Zadrozny, K. K.; Xu, C.; Schur, F. K. M.; Lyddon, T. D.; Riccana, C. L.; Wagner, J. M.; Perilla, J. R.; Ganser-Pornillos, B. K.; Johnson, M. C.; et al. Inositol phosphates are assembly cofactors for HIV-1. *Nature* **2018**, *560*, 509−512.
(59) Liu, C.; Perilla, J. R.; Ning, J.; Lu, M.; Hou, G.; Ramalho, R.; Himes, B. A.; Zhao, G.; Bedwell, G. J.; Byeon, I.-J.; Ahn, J.; Gronenborn, A.; Prevelige, P.E.; Rousso, I.; Aiken, C.; Polenova, T.; Schulten, K.; Zhang, P. Cyclophilin A stabilizes the HIV-1 capsid through a novel non-canonical binding site. *Nat. Commun.* **2016**, *7*, 10714.
(60) Levandovsky, A.; Zandi, R. Nonequilibrium assembly, retroviruses, and conical structures. *Phys. Rev. Lett.* **2009**, *102*, 198102.
(61) Zandi, R.; Dragnea, B.; Travesset, A.; Podgornik, R. On virus growth and form. *Phys. Rep.* **2020**, *847*, 1−102.
(62) Šali, A.; Blundell, T. L. Comparative Protein Modelling by Satisfaction of Spatial Restraints. *J. Mol. Biol.* **1993**, *234*, 779−815.
(63) Gordon, J. C.; Myers, J. B.; Folta, T.; Shoja, V.; Heath, L. S.; Onufriev, A. H++: A Server for Estimating pKas and Adding Missing Hydrogens to Macromolecules. *Nucleic Acids Res.* **2005**, *33*, W368−W371.
(64) Case, D. A.; Aktulga, H. M.; Belfon, K.; Cerutti, D. S.; Cisneros, G. A.; Cruzeiro, V. W. D.; Forouzesh, N.; Giese, T. J.; Götz, A. W.; Gohlke, H.; Izadi, S.; Kasavajhala, K.; Kaymak, M. C.; King, E.; Kurtzman, T.; Lee, T.-S.; Li, P.; Liu, J.; Luchko, T.; Luo, R.; Manathunga, M.; Machado, M. R.; Nguyen, H. M.; O'Hearn, K. A.; Onufriev, A. V.; Pan, F.; Pantano, S.; Qi, R.; Rahnamoun, A.; Risheh, A.; Schott-Verdugo, S.; Shajan, A.; Swails, J.; Wang, J.; Wei, H.; Wu, X.; Wu, Y.; Zhang, S.; Zhao, S.; Zhu, Q.; Cheatham, T. E.; Roe, D. R.; Roitberg, A.; Simmerling, C.; York, D. M.; Nagan, M. C.; Merz, K. M. AmberTools. *J. Chem. Inf. Model.* **2023**, *63*, 6183−6191.
(65) Maier, J. A.; Martinez, C.; Kasavajhala, K.; Wickstrom, L.; Hauser, K. E.; Simmerling, C. ff14SB: Improving the Accuracy of Protein Side Chain and Backbone Parameters from ff99SB. *J. Chem. Theory Comput.* **2015**, *11* (8), 3696−3713.
(66) Jorgensen, W. L.; Chandrasekhar, J.; Madura, J. D.; Impey, R. W.; Klein, M. L. Comparison of Simple Potential Functions for Simulating Liquid Water. *J. Chem. Phys.* **1983**, *79*, 926−935.
(67) Machado, M. R.; Pantano, S. Split the Charge Difference in Two! A Rule of Thumb for Adding Proper Amounts of Ions in MD Simulations. *J. Chem. Theory Comput.* **2020**, *16*, 1367−1372.
(68) Eastman, P.; Swails, J.; Chodera, J. D.; McGibbon, R. T.; Zhao, Y.; Beauchamp, K. A.; Wang, L.-P.; Simmonett, A. C.; Harrigan, M. P.; Stern, C. D.; Wiewiora, R. P.; Brooks, B. R.; Pande, V. S OpenMM 7: Rapid Development of High Performance Algorithms for Molecular Dynamics. *PloS Comput. Biol.* **2017**, *13*, No. e1005659.
(69) Roe, D. R.; Cheatham, T. E. PTRAJ and CPPTRAJ: Software for Processing and Analysis of Molecular Dynamics Trajectory Data. *J. Chem. Theory Comput.* **2013**, *9*, 3084−3095.
(70) Humphrey, W.; Dalke, A.; Schulten, K. VMD: Visual Molecular Dynamics. *J. Mol. Graph.* **1996**, *14*, 33−38.


https://doi.org/10.1021/acsnano.4c07948
*ACS Nano* 2024, 18, 27465−27478